

Analysis of four-dimensional variational state estimation of the Hawaiian waters

D. Matthews,¹ B. S. Powell,¹ and I. Janeković^{1,2}

Received 3 September 2011; revised 6 January 2012; accepted 9 January 2012; published 9 March 2012.

[1] In this study, we evaluate results from an incremental strong constraint four-dimensional variational data assimilation (IS4D-Var) experiment applied to the circulation around the Hawaiian Islands using the Regional Ocean Modeling System (ROMS). Assimilated observations include (1) satellite-derived high-resolution swath radiometer sea surface temperatures (SST) and along-track altimetric sea surface heights (SSH) and (2) in situ temperature and salinity profiles from Argo floats, autonomous Seagliders, and shipboard conductivity-temperature-depth. Two assimilation configurations are compared: adjusting initial conditions versus adjusting both initial conditions along with atmospheric forcing. In the latter case, we compare two separate forcing products. For all experiments, we investigate how the assimilation alters the tidal, inertial, and mesoscale variability. Significant improvements in the observation-model fit are found for SST and salinity regardless of assimilation configuration or atmospheric forcing; however, significant change to the subsurface temperature is made when adjusting only initial conditions. Baroclinic tides are altered during the assimilation because of changes in the density field in regions of strong internal tide generation. Spurious inertial oscillations are found in assimilation circulations that are associated with the IS4D-Var increment when using either SST or SSH observations; however, this increase in the inertial energy had minimal effect on the mesoscale variability.

Citation: Matthews, D., B. S. Powell, and I. Janeković (2012), Analysis of four-dimensional variational state estimation of the Hawaiian waters, *J. Geophys. Res.*, 117, C03013, doi:10.1029/2011JC007575.

1. Introduction

[2] Data assimilation is the process of combining observations and a numerical model to produce an optimal estimate of the system. The goal of time-dependent four-dimensional variational assimilation (4D-Var) is to use the dynamics of the model to determine an initial state, boundary conditions, and atmospheric forcing that minimize a scalar function measuring the distance to the observations [Talagrand and Courtier, 1987; Courtier et al., 1994]. The incremental approach, which is an approximation to 4D-Var, allows for a significant improvement to the cost-benefit trade-off by working with linear increments to the state [Courtier et al., 1994]. A complete 4D-Var system has been developed within the Regional Ocean Modeling System (ROMS) model and is comprehensively described by Moore et al. [2011c]. In this study, we employ the incremental strong constraint 4D-Var (IS4D-Var) to adjust the initial conditions and atmospheric forcing, assuming that the model physics do not contain errors. The mentioned ROMS IS4D-Var system has been previously used to study ocean

dynamics in several regions [Powell et al., 2008; Broquet et al., 2009; Zhang et al., 2010; Moore et al., 2011a, 2011b].

[3] Our model domain covers the Hawaiian Islands (Figure 1) located in the southern portion of the North Pacific Gyre, characterized with the presence of nearly persistent northeastward trade winds that have a significant effect on both ocean currents and winds [Xie et al., 2001]. The mountain peaks on the islands of Maui and Hawai'i penetrate the trade wind inversion layer, deflecting the wind flow around the islands, creating a large wake region of weakened flow [Smith and Grubii, 1993]. An active and intense eddy field lies in the wake region (Figure 1b), driven primarily by the wind stress curl and intrinsic instabilities in the ocean flow [Calil et al., 2008; Yoshida et al., 2010]. Variability is also increased because of both baroclinic and barotropic instabilities in the mean flow [Chen and Qiu, 2010] in the northwest of the domain. Furthermore, the Hawaiian Islands are a significant site for the generation of internal waves because of tidal flow over steep topography [Merrifield et al., 2001; Ray and Mitchum, 1996]. Vertical tidal motions of the thermocline are commonly observed in the region with amplitudes of over 10 m [Chiswell, 1994] and can peak above 90 m along tidal beams that originate on both sides of the ridge [Carter et al., 2008].

[4] The North Equatorial Current (NEC) flows from east to west, intensifying in the southward direction east of the island chain (Figure 1a). The mean ocean circulation in lee

¹Department of Oceanography, University of Hawai'i at Mānoa, Honolulu, Hawaii, USA.

²On leave from Institute Rudjer Bošković, Zagreb, Croatia.

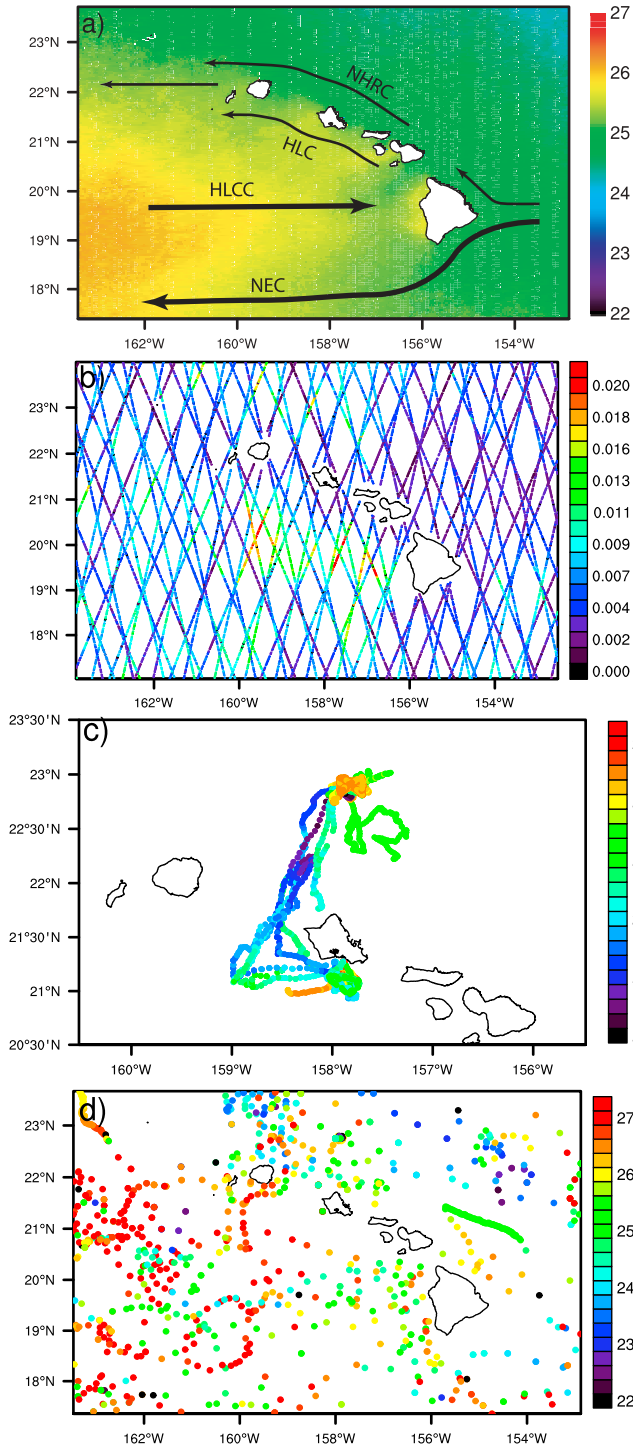


Figure 1. (a) Time-averaged map from satellite observations of SST at the model grid and (b) temporal variance of SLA observations, (c) temperatures above 20 m depth layer from Seagliders, and (d) Argo and shipboard profiles.

of the islands forms a canonical pattern [Lumpkin, 1998; Flament et al., 1998] with four major current systems. The NEC impinges on the island of Hawai'i and bifurcates, with most of the current flowing southwest past the island chain. The North Hawaiian Ridge Current (NHRC) flows northwest along the windward side of the islands. Along the

leeward side of the island chain, from Maui to Kaua'i, the Hawaiian Lee Current (HLC) flows northwest, parallel to the NHRC. The Hawaiian Lee Counter Current (HLCC), which forms in response to the wind stress wake of the islands, flows counter to the NEC [Xie et al., 2001] along 19°N. Surface water temperatures in the region have a strong meridional gradient and a slight zonal gradient (Figure 1a), with warmer water in the southwest because of the HLCC [Lumpkin, 1998] having an annual cycle variation between an average of 23°C in winter and 27°C in summer.

[5] The main objective of this study is to examine the skill and performance of the data assimilation system for the Hawaiian ocean state modeled at a submesoscale resolution by producing analyses of the dynamics over a two year time period (2008–2010). The assimilation system experiment uses two different configurations: in 2008 only the initial conditions of the model are adjusted, while in 2009, both the initial conditions and the atmospheric forcing are adjusted. Broquet et al. [2011] showed that without surface forcing adjustment the assimilation could degrade the temperature structure at depth; however, adjusting the surface forcing can lead to abnormal temporal and spatial variability in the forcing fields. In our study, we assimilate a significant number of remote and in situ observations of the circulation, including: high-resolution, minimally processed, non-blended (temporally or spatially) satellite observations using validated sea surface temperature (SST) swath data and along-track sea surface height (SSH) data, along with in situ temperature and salinity data from autonomous Seagliders, Argo floats, and shipboard conductivity, temperature, salinity (CTD) profiles.

[6] We evaluate the performance of an IS4D-Var system in a complex island domain with strong barotropic and baroclinic tides, large mesoscale eddies, complex submesoscale interactions, and dominant atmospheric forcing by comparing how well the model can reproduce the observations within the consistency of the errors. Furthermore, we compare the dynamical adjustments made to the model when perturbing either or both the initial conditions and atmospheric forcing. Finally, we discuss the resulting circulation and how adjustments affect the estimates of the tides, inertial, and mesoscale flows. Each of these objectives is presented below, followed by concluding remarks at the end.

2. Data Assimilation System

2.1. IS4D-Var Theory

[7] For our study, we utilize the IS4D-Var system within ROMS model based on the formulation of Courtier et al. [1994], using the adjoint and tangent linear models [Moore et al., 2004, 2011c]. In this section, we briefly present the principles of IS4D-Var, encouraging the reader to the more detailed description by Moore et al. [2011c]. The 4D-Var system has several advantages over other methods used to combine observations with an ocean model, such as optimal interpolation (OI) or 3D-Var. Our goal is not to compare the relative merits of each, but a review is given by Lorenc [2006]. The two main advantages of 4D-Var are that the time-variable dynamics of the model are used to evolve the error covariances and more observational constraints are available during a time window as opposed to a single time. These characteristics of 4D-Var are essential for this study

because of the strong internal tides that generate significant baroclinic velocities in the region and can heave the thermocline by as much as 90 m during a single M_2 cycle [Carter et al., 2008]. The direction of baroclinic energy flux from the ridges is partially dependent upon the spatiotemporal variations of the background stratification that requires the full model physics to resolve. Further complicating the matter is the use of Seaglider and Argo data sets that sample in both space and time, preventing us from removing baroclinic tides from the observations.

[8] The system is applied to time cycles of interval $[t_o, t_f]$, during which the model control variables (initial conditions, $\mathbf{x}(0)$, surface forcing, $\mathbf{f}(t)$, and boundary conditions, $\mathbf{x}_{bc}(t)$) are corrected to ensure that the model better agrees with the observations in a least squares sense. The incremental form determines the linear increments, $\delta\mathbf{z} = (\delta\mathbf{x}(0), \delta\mathbf{f}(t), \delta\mathbf{x}_{bc}(t))$ that should be applied to the control vector. These linear increments are integrated forward in time with the tangent linear model, while the sensitivity of the quadratic cost function to the increments is determined by the adjoint model.

[9] The quadratic cost function that describes the difference to be minimized is defined as the combined penalty for deviating from the observations (\mathcal{J}_o) and initial guess (\mathcal{J}_b), as given by

$$\mathcal{J}_o = \frac{1}{2}(\mathbf{G}\delta\mathbf{z} - \mathbf{d})^T \mathbf{R}^{-1} (\mathbf{G}\delta\mathbf{z} - \mathbf{d}) \quad (1)$$

$$\mathcal{J}_b = \delta\mathbf{x}(0)^T \mathbf{P}_b^{-1} \delta\mathbf{x}(0) + \delta\mathbf{f}(t)^T \mathbf{P}_f^{-1} \delta\mathbf{f}(t) + \delta\mathbf{x}_{bc}(t)^T \mathbf{P}_{bc}^{-1} \delta\mathbf{x}_{bc}(t). \quad (2)$$

where \mathbf{P}_b , \mathbf{P}_f , \mathbf{P}_{bc} , and \mathbf{R} are the assumed background, forcing, boundary condition, and observation error covariance matrices, \mathbf{G} is the tangent linear model sampled at the observation locations, \mathbf{G}^T is the adjoint of \mathbf{G} , and \mathbf{d} (or innovation vector) is the difference between the first guess and the observations. The optimal increment $\delta\mathbf{z}^*$ that minimizes \mathcal{J} is calculated using an iterative Lanczos formulation of the Conjugate Gradient (CG) algorithm [Fisher, 1998].

2.2. Model Configuration

[10] We model the Hawaiian Island region at a 4 km resolution with 30 s levels, with ROMS, a free surface, hydrostatic, primitive equation model discretized with a terrain following vertical coordinate system [Shchepetkin and McWilliams, 2005]. The domain spans 164°W to 153°W in longitude and 17°N to 24°N in latitude. The model bathymetry is based upon data from the Hawaiian Mapping Research Group, though slightly adjusted to minimize the effects of horizontal pressure gradient errors (HPGE). The mean HPGEs were found to be less than 7 cm/s around the island chain. The baroclinic time step is 450 s, and the barotropic time step is less than 12 s because of the deep depths in the domain. The boundary conditions are configured to conserve volume using a Chapman condition of the free surface [Chapman, 1985], a Flather condition for the 2D momentum, and clamped for the 3D momentum and tracers [Marchesiello, 2001]. A fourth-order Akima horizontal advection scheme is used

[Akima, 1984], along with the KPP vertical mixing scheme described by Large et al. [1994].

[11] The lateral boundary conditions are taken from Navy Coastal Ocean Model (NCOM) fields supplied by the Naval Research Laboratory (NRL) [Barron et al., 2006]. Because of imbalances between NCOM and ROMS we employ a sponge layer along the four boundaries with a width equal to one Rossby radius of deformation of the region (80 km). The model was additionally forced with eight primary (M_2 , S_2 , N_2 , K_2 , K_1 , O_1 , P_1 , Q_1), two long-period (M_f , M_m), and one nonlinear (M_4) barotropic tidal constituents from the Oregon State University TOPEX/Poseidon tidal product, TPXO7.1 [Egbert et al., 1994] in all experiments. There are two distinct periods using differing atmospheric forcing products in our study: the first, is a combination of the NCEP-CORA wind product [Milliff et al., 2004] that combines NCEP winds (2°) with observed Quikscat winds (0.5°) that we have combined with winds from a fine-scale (9 km) PSU/NCAR mesoscale model (MM5) [Yang et al., 2008a]. The MM5 winds are statistically blended with the NCEP-CORA winds to cover a domain larger than the available MM5 data. The other NCEP fields for temperature, humidity, pressure, rain, and heat flux are used at the coarse 2° resolution. The second, from July of 2009, is a locally run, high-resolution Weather Regional Forecast (WRF) model that covers the entirety of the domain. The ROMS ocean surface heat flux is computed via the COARE algorithm of Fairall et al. [1996] using information from the atmospheric models. We apply a monthly mean heat flux correction to balance the climatological NCOM SST with either MM5 or WRF, depending on the period of simulation, to account for any heat flux imbalance between the state of the ocean and the atmospheric forcing. This correction is made to balance the incoming boundary conditions which are in balance with a different atmosphere than those forced with the global NCEP fluxes.

2.3. Observations

[12] Observational data are taken from all available products at their native resolutions, with satellite SST and SSH providing observations of the ocean surface, while shipboard CTD, ARGO floats, and autonomous Seagliders provide observations of the ocean interior.

[13] SST observations are taken from the Global Ocean Data Assimilation Experiment High Resolution Sea Surface Temperature (GHRSST) Level 2 Preprocessed (L2P) sea surface temperature data set distributed by the Physical Oceanography Distributed Active Archive Center (PO. DAAC) from both the advanced very high resolution radiometer (AVHRR) and the Moderate Resolution Infrared Spectroradiometer (MODIS) sensors. These observations have a 1.1 km spatial resolution and give estimates of SST that are nominally accurate to 0.5°C [McClain et al., 1985]. The MODIS sensor is onboard the polar orbiting NASA AQUA and TERRA satellites with timed orbits such that TERRA passes from north to south across the equator in the morning and AQUA passes in the afternoon. This setup provides two primary satellite passes per day at approximately 02:00 and 14:00 local time; however, because of the large swath, multiple passes of the satellite capture portions of our domain. A higher number of SST observations are available in lee of the islands because of the westerly

reversal blocking of the winds that keep the island wakes cool and nearly free of clouds during the day [Yang *et al.*, 2008a].

[14] We also use the along-track sea level anomaly (SLA) product produced by Ssalto/Duacs and distributed by Archiving Validation and Interpretation of Satellite Oceanographic data (AVISO), with support from Centre National d'Etudes Spaciales (CNES), from the altimeters onboard the Jason-1, Jason-2, Envisat, and Geosat Follow On (GFO) satellites. The along-track resolution is ~ 6 km for Jason-1 and Jason-2, ~ 7 km for Envisat, and ~ 10 km for GFO (Figure 1b). The cross-track resolution varies depending on the satellites overhead and their current orbital path. A mean sea surface from a 6 year run of the nonlinear model was added to the SLA data to generate SSH data that are consistent with the model free surface. We do not want to adjust the TPXO tidal forcing during assimilation, hence predicted tides from the nonlinear model are added to the SLA observations such that tidal frequency signals should not be considered in the assimilation cycle. One caveat in the assimilation of SSH data is that the adjoint model may identify a sensitivity to gravity waves that are capable of resolving the model and observation difference [see Powell *et al.*, 2009]. Although dynamically correct, spurious gravity waves are not an appropriate signal to be added during the assimilation. To prevent this, we replicate each altimeter observation at $t = [t_o - 6, t_o - 4, t_o - 2, t_o, t_o + 2, t_o + 4, t_o + 6]$ hours, but with the appropriate tidal elevation. Here we assume high temporal correlation of the subtidal altimeter data, as the sampled altimeter mesoscale field does not change significantly over 12 h.

[15] For this experiment, in situ depth profiles of temperature and salinity are provided by three different platforms: Argo floats, autonomous Seagliders, and shipboard CTD. The Argo program is a global array of vertical profiling floats that provide temperature and salinity profiles every 10 days at depths ranging from the surface to 2000 m [Oka and Ando, 2004]. We only use data during the ascension and descension of the Argo float (locations of Argo surfacings are shown in Figure 1d), during which samples are taken every 10 m vertically. The University of Hawai'i operates a number of autonomous, buoyancy driven Seagliders in the region that are capable of predefined mission dives and can sample temperature and salinity from the surface to 1000 m. The Seaglider missions used were part of the Hawai'i Ocean Time-series (HOT) program [Karl and Lukas, 1996] and Hawai'i Ocean Observing System (HiOOS) primarily around the island of O'ahu (Figure 1c). Because of the nature of the Seaglider motion, horizontal and vertical resolutions are variable. Also from the HOT program, we utilize temperature and salinity profile data from monthly HOT cruises taken to the deepwater station A Long-Term Oligotrophic Habitat Assessment (ALOHA) site located 100 km north of the island of O'ahu.

[16] Because a majority of the considered observations are at a higher spatial resolution than the model, observations are spatially averaged into bins that relate to the grid cells of the model, while preserving the time of observation. This procedure removes small-scale features in the observations, not represented by the model, and allows for an error of representativeness to be estimated from the observational variance present in each bin. All observations within a

Rossby radius distance from the model open boundaries are removed from consideration because of the strong sponge layer in the region to mitigate inconsistencies with the boundary conditions.

[17] In IS4D-Var the difference between each observation and model is weighted by the observation error of representativeness covariance matrix (\mathbf{R}); although, it is formally a covariance matrix, we use a diagonal variance matrix of size equal to the number of observations. The variance assigned to each observation is the maximum of either: the variance calculated from the gridding procedure above, the instrument error or the geophysical time-variability of each observational product. The noise level was found using a semivariogram technique [Matthews *et al.*, 2011] or from a residual spectra method [Zanifé *et al.*, 2003]. An estimate of the geophysical time variance was found from multiple year time series of each observation product. In the case of SST, we generated monthly maps of variance using 5 years of daily global level 3 MODIS and pathfinder AVHRR data provided by PO.DAAC. Monthly maps of SSH variance were generated using all data from each satellite starting after January 2000. For in situ observations, variance was calculated as a function of depth using 20 m bins from the surface to the maximum depth. Temperature and salinity data from 20 years of HOT profiles, 8 years of Argo profiles, and 2 years of various Seaglider missions were used to estimate the geophysical variance for each of the observation platforms.

[18] We only used MODIS data to provide SST because of the large number of SST observations; however, from March 2009 to June 2009 the MODIS data was cloud contaminated, as many observations were too cold for the tropics (less than 18°C). We assimilated only SST data from AVHRR NOAA 18 during this period. The cloud filter problem was resolved by July 2009 and MODIS data were used for the remainder of the study. Finally, the primary AVISO high-resolution, along-track data is provided in delayed time. At the time of these experiments, the data were only available through July 2009, after which the AVISO near-real-time, variable along-track (~ 20 km) resolution product was used, resulting in far fewer SSH observations.

[19] After the gridding procedure, nearly 27 million observations were created for the two year period, of which 94.5% were SST from satellite radiometers, 3.7% from SSH altimetry, and 1.65%, 0.1%, and 0.4% were temperature and salinity observations from Seagliders, Argo floats, and HOT cruise CTD, respectively. Our goal is to use as many available data (particularly, in situ), but by withholding AVHRR data we are able to examine the assimilation system against an independent set of observations.

2.4. Data Assimilation Setup

[20] There are several parameters required to be determined *a priori* to the assimilation. The length of the assimilation time cycle should not exceed the period for which the tangent linear assumption is valid for incremental 4D-Var methods. A particularly energetic period was chosen (12–19 July 2008) to perform an ensemble experiment to determine this time length. Orthonormal perturbations were generated (as per Powell *et al.* [2008]) and integrated separately by the nonlinear and tangent linear models. Ensemble root-mean-square (RMS) and correlations between the perturbed

Table 1. Summary of Numerical Experiments Used in This Study

Name	Description	Time Period
FWD	Forward model with no assimilation	1 Jan 2008 to 4 Jan 2010
NF08	Assimilation, no forcing adjustment, forcing from MM5/NCEP	1 Jan 2008 to 1 Jan 2009
F09M	Assimilation, forcing adjustment, forcing from MM5/NCEP	2 Jan 2009 to 16 Jul 2009
F09W	Assimilation, forcing adjustment, forcing from WRF	16 Jul 2009 to 4 Jan 2010

nonlinear (NLM) and tangent linear (TLM) solutions were then compared to determine consistency. The assumption of linearity is no longer valid once the solutions deviate, providing an estimate of the maximum time that should be used for the assimilation window. The results showed that after 4.5 to 5 days the NLM and the TLM are no longer consistent. A 4 day assimilation cycle length was chosen for all experiments from this information.

[21] Twenty inner loops were used for the experiments, as further loops provided little reduction in the cost function. For some periods, because of strong tidal currents along steep slopes, the model time step was reduced to maintain the CFL condition. The number of inner loops was slightly reduced such that the total integration time was similar during these periods.

[22] The background and forcing error covariance matrices (equation (2)) constrain the analysis by penalizing departures from the background state. Estimating \mathbf{P}_b , and \mathbf{P}_f is accomplished through factorization [Weaver and Courtier, 2001]. Because the covariance terms are not known directly, they are approximated by a Gaussian diffusion of the standard deviations over specified length scales. The standard deviations were computed from monthly climatologies on the basis of a 6 year run of the NLM, such that each cycle used its monthly variance. Background length scales for the diffusion were calculated using the semivariogram technique on multiyear time series of satellite and in situ data sets described in detail by Matthews et al. [2011]. Horizontal length scales of 150 km were chosen for free surface and velocity with 170 km for temperature and salt. Vertical length scales were set to 50 m for velocity, 140 m for temperature, and 240 m for salt. Surface forcing length scales were set to 50 km for wind stress and 250 km for heat and salt flux.

2.5. Experiment Setup

[23] This IS4D-Var experiment of circulation around the Hawaiian Islands is performed for the period of 1 January 2008 through 31 December 2009. We compare the IS4D-Var system to a control run without data assimilation (deemed FWD) through statistical measures of model performance. The assimilation experiment is performed in two stages. In 2008, only initial conditions are adjusted during the assimilation cycles (deemed NF08), while in 2009, initial conditions are adjusted and surface forcing is corrected every 12 h (deemed F09). Because of the switch in atmospheric forcing in July 2009, we decompose the F09 experiment into F09M, which refers to the analysis circulations with forcing adjustment and MM5/NCEP forcing, and F09W, which refers to the analysis circulations with forcing

adjustment and WRF forcing. The experiments are summarized in Table 1.

3. Results

3.1. Comparison Between the Model Experiments and Observations

[24] In this section, we explore the effects of the different assimilation configurations, atmospheric forcings, and observational products on the model performance. Over the 2 year study period the observational contribution to the cost function is 86.1%, 3.4%, 3.9%, and 6.2% for SST, temperature at depth, salinity, and SSH, respectively. The assimilation system reduces the root mean squared error (RMSE) between observations and the model by 0.21 K, 0.21 K, 0.072, and 0.013 m, which corresponds to a reduction of 37%, 22%, 40%, and 12%, in SST, temperature at depth, salinity, and SSH, respectively, as compared against the FWD case. While the correlation coefficient (CC) between the observations and the model are high in the FWD experiment (above 0.89), the assimilation still makes improvements of 3%, 0.5%, 3.1%, and 1.4% for SST, temperature at depth, salinity, and SSH, respectively.

[25] Comparing the assimilation system against the AVHRR SST data withheld during the assimilation, we find that it reduces the total RMSE by 0.1 K compared to the FWD experiment and increases the correlation from 0.94 to 0.95. However, significantly larger corrections are found directly in lee and south of the island of Hawai'i and in the Alenuihaha Channel (between Maui and Hawai'i), where RMSE is reduced from the FWD experiment by over 0.4 K.

[26] Figure 2 shows the RMSE between the model and observations, with the average observational error assigned for each 4 day assimilation cycle. Similarly, Figure 3 shows the CC between the model and observations for each 4 day cycle. The average observational error assigned to the delayed time SSH data is 5.5 and 6.5 cm for the near real-time product. The SSH RMSE shows no trend until the switch to real-time data on 17 July 2009, at which the RMSE between the observations and the FWD experiment increases by 2 cm because of a reduction of quality control in the real-time data (Figure 2a). Because the change in SSH observational products nearly coincides with the change in the atmospheric forcing, we conducted a short additional 36 day test to determine whether the change in forcing may also be contributing to the increased RMSE. Our findings show that during the test period, the SSH RMSE was unaffected by the change in atmospheric forcing. Also, no significant difference in SSH RMSE is found when comparing NF08 and F09M. The reduction of RMSE between the FWD and analyses is limited to an average of 11.6 cm (improvement of 4.6%) when using the near real-time data, compared to 9.4 cm from the delayed-time product (improvement of 12.5%). The average reduction of RMSE from Jason-1 and Jason-2 (15.4% and 14.9%) is larger than that from Envisat and GFO (9.6% and 7.4%). This is likely due to an increase in noise levels in the Envisat and GFO data relative to Jason-1 and Jason-2, which from residual spectral methods was found to be 2 cm larger. The SSH CC for the experiments are: FWD 0.88, NF08 0.89, F09M 0.91, and F09W 0.85.

[27] The RMSE between the SST and FWD increases in 2009 because of the change from MM5/NCEP to WRF for

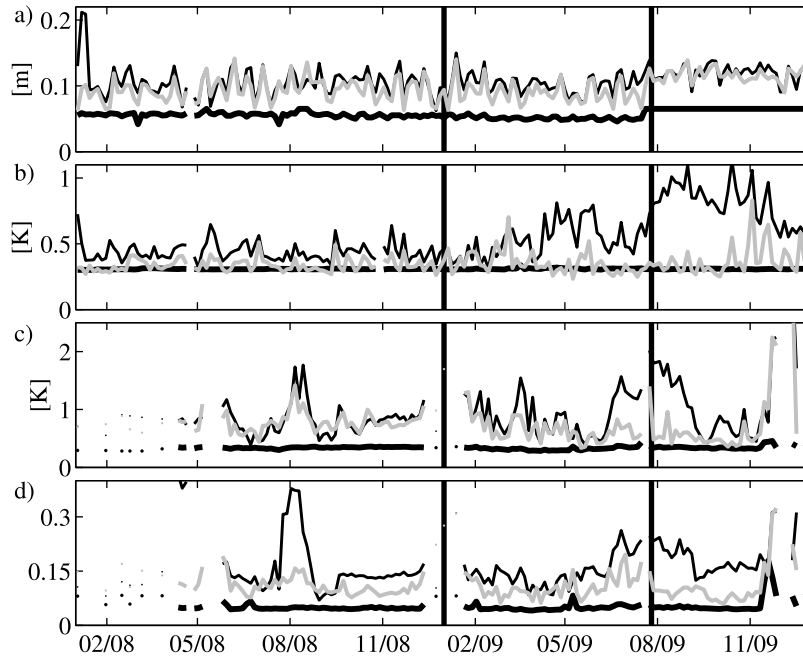


Figure 2. Time series of root-mean-square error (RMSE) between the model (FWD experiment shown by thin black line, and NF08, F09M, and F09W shown with thin grey line) and observations of (a) sea surface height (SSH), (b) sea surface temperature (SST), (c) temperature below surface, and (d) salinity per experiment cycle. The mean observational error per cycle is shown by the thick dashed line. The time periods of the NF08, F09M, and F09W experiments are shown by the vertical lines.

atmospheric forcing on 26 July 2009 (Figure 2b). The average SST RMSE from FWD is 0.41, 0.52, and 0.79 K during the NF08, F09M, and F09W periods. All assimilation experiments reduced the SST RMSE to average values of 0.34, 0.35, and 0.39 K for NF08, F09M, and F09W,

respectively, which is close to the average SST observational error of 0.31 K. Figures 4a and 4b shows a map of SST RMSE from FWD and a combination of the NF08, F09M, and F09W experiments, respectively. The highest errors in FWD, with values greater than 0.8 K, are found in the lee of

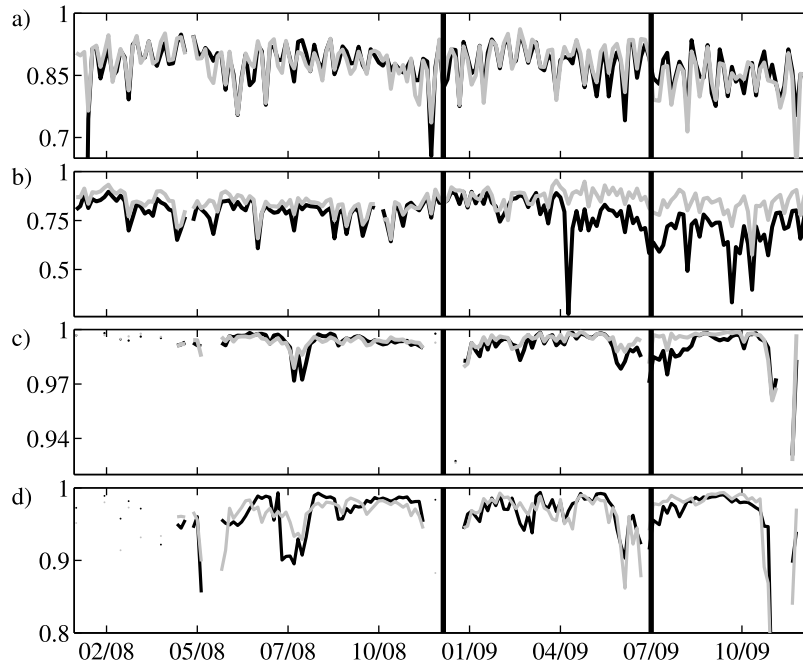


Figure 3. Correlation coefficients computed over each cycle between the model (FWD shown with black line, and NF08, F09M, and F09W shown by grey lines) and observations for (a) SSH, (b) SST, (c) subsurface temperature, and (d) salinity. Vertical lines are as in Figure 2.

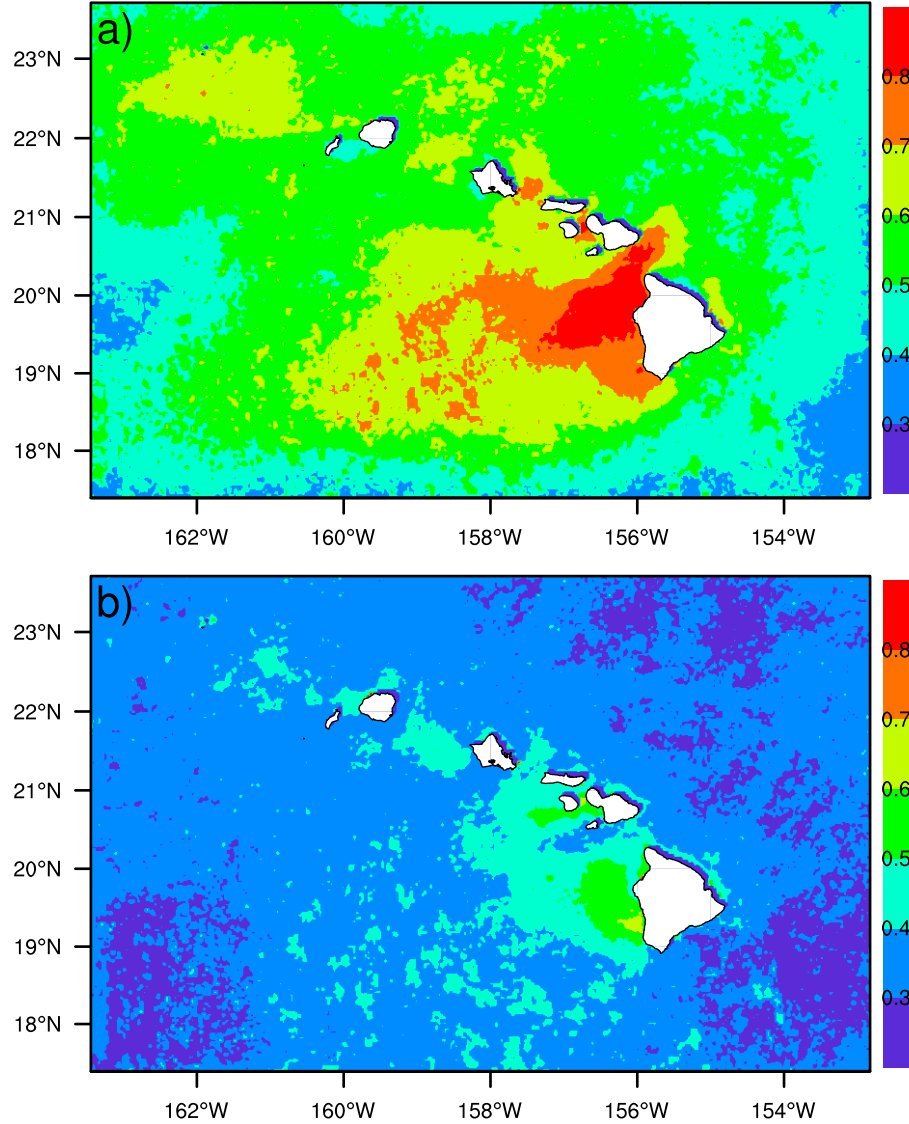


Figure 4. (a) Time-averaged SST RMSE (K) from FWD and (b) assimilation experiments based on the 2 year study period.

the island of Hawai'i and in the Alenuihaha Channel. Decorrelation length scales are reduced and variability is increased [Matthews et al., 2011] in lee of the island of Hawai'i; also, there is a strong diurnal variation in SST due to increased variability in heat flux from a reduction in cloud cover [Yang et al., 2008b]. The assimilation reduces the RMSE for SST to less than 0.4 K away from the Hawaiian lee and to less than 0.6 K in the lee in all assimilation experiments. Overall, the state estimation is performing exceptionally well with respect to the SST; however, the strong diurnal variability in the lee is not adequately captured by the models. We address the comparison between model and observed SST in detail in section 3.3.

[28] RMSE between the experiments and in situ temperature observations are shown in Figure 2c. For subsurface temperature, the average RMSE is 0.78, 0.74, and 0.63 K for NF08, NF09M, and NF09W, respectively. This is a reduction of 6%, 26%, and 42% as compared to FWD. The in situ observational error is primarily chosen to be the instrument

error. These observations are taken in regions of strong baroclinic tides that heave the isopycnals by as much as 100 m [Carter et al., 2008]. A numerical model with coarser resolution and bathymetry than reality will not capture the precise phase of the baroclinic tide; hence, an internal wave with a 5 min phase shift can result in significant differences between the in situ and modeled values. On reflection, using the instrument error to capture the representation of in situ observations was a mistake, but rather an error should have been used that is indicative of possible phase changes in propagating internal tides. Large reductions of in situ salinity RMSE, compared to FWD, are found (Figure 2d) in each assimilation experiment, with values of 45%, 55%, and 47% in NF08, F09M, and F09W, respectively. We relaxed the surface salinity flux toward climatology in the NF08 experiment, which introduced a 0.2 reduced salinity bias when compared to observations in the mixed layer of the FWD experiment. This bias then was reduced to 0.15 in the NF08 experiment. Significant variability exists in the reduction of

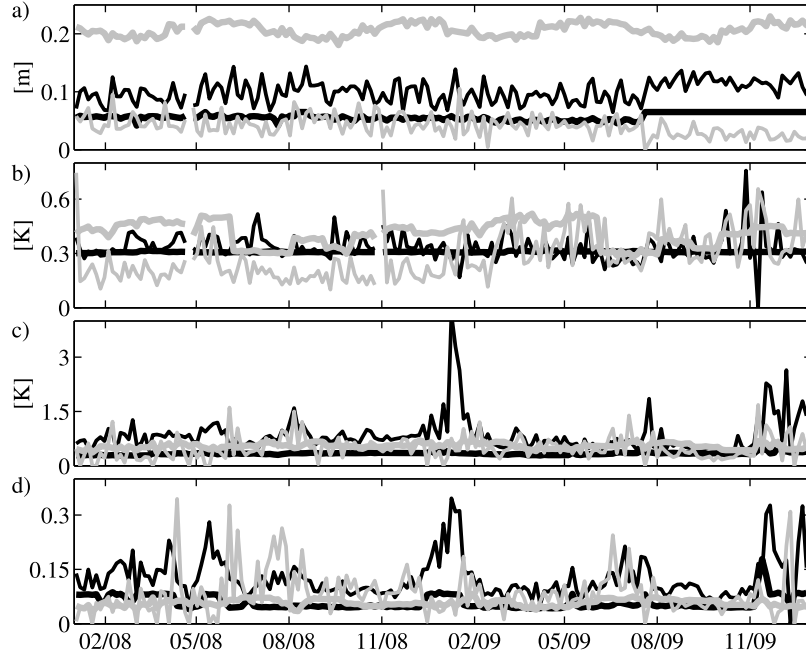


Figure 5. Time series of spatially averaged a priori background errors (thick grey line) and observation (thick black line) standard deviations. Time series of posterior background (thin grey line) and observation (thin black line) standard deviations computed from equation (3) and (4). Values are for (a) SSH, (b) SST, (c) subsurface temperature, and (d) salinity.

RMSE, when compared to FWD, between the different in situ platforms. The Seaglider observations dominate the number of in situ observations when they are available and provide the greatest reduction in RMSE.

3.2. Consistency of Background Error Covariance

[29] We examine the consistency of our specified error covariance matrices using a set of diagnostics described by Desroziers *et al.* [2009] and Moore *et al.* [2011a]. These diagnostics are based on the innovation vector and consider the projection of the background and analysis into observation space. Desroziers *et al.* [2009] determine the posterior observation and background error variances using

$$(\tilde{\sigma}_i^b)^2 = \frac{1}{2} \sum_{j=1}^{p_i} (\mathbf{y}_j^a - \mathbf{y}_j^b)(\mathbf{y}_j^o - \mathbf{y}_j^b) \quad (3)$$

$$(\tilde{\sigma}_i^o)^2 = \frac{1}{2} \sum_{j=1}^{p_i} (\mathbf{y}_j^o - \mathbf{y}_j^a)(\mathbf{y}_j^o - \mathbf{y}_j^b) \quad (4)$$

where i refers to the observation type, p_i is the number of observations of that type, and \mathbf{y}_j^a , \mathbf{y}_j^b , and \mathbf{y}_j^o refer to the analysis, background, and observation values, respectively. If the prior background and observation error covariance matrices are well specified, they will be consistent with the posterior values $(\tilde{\sigma}_i^b)^2$ and $(\tilde{\sigma}_i^o)^2$. Figure 5 shows the time series of the posterior errors from the 2 year assimilation experiments against the prior errors for the same observation points for salinity, SSH, SST (from satellite observations),

and subsurface temperature (from in situ observations). For SSH, we found that the observation prior and posterior errors ($\tilde{\sigma}_i^o > \tilde{\sigma}_i^b$) are consistent within a factor of 2, such that the prior is underestimating the actual error. As described earlier, the covariances were artificially increased when adding the TPXO tides, and it seems that too much error was attributed. Worse, the background prior covariance did not remove the tidal signal, and so the background covariance error is significantly overestimated for SSH. For SST, the observation prior and posterior errors are consistent (Figures 5c and 5d), while the prescribed diurnal variance in the background is an overestimate of what is found in the posterior. For the in situ measurements, the variances used were all consistent and the overall results are consistent with those reported in both meteorological and oceanographic applications using data assimilation [Moore *et al.*, 2011a]. The diagnostics suggest that improvements in the analysis would be seen if the SSH observation errors were increased and the background errors were decreased. This would affect the cost function by giving less weight to the innovation vector and reduce the penalties on differences between the analysis and background. However, one must keep in mind that the diagnosed observation and background errors shown in Figure 5 are not the true or optimal values, depending on the a priori choices of the errors, but can be used to characterize the priori estimates.

3.3. Temperature and Heat Flux Adjustments

[30] In this section, we focus on the analysis of the assimilating high-resolution satellite radiometry derived SST (that account for over 94% of all observations considered), in order to understand the differences in performances of the NF08 and the F09(M/W) experiments. The 4D-Var theory

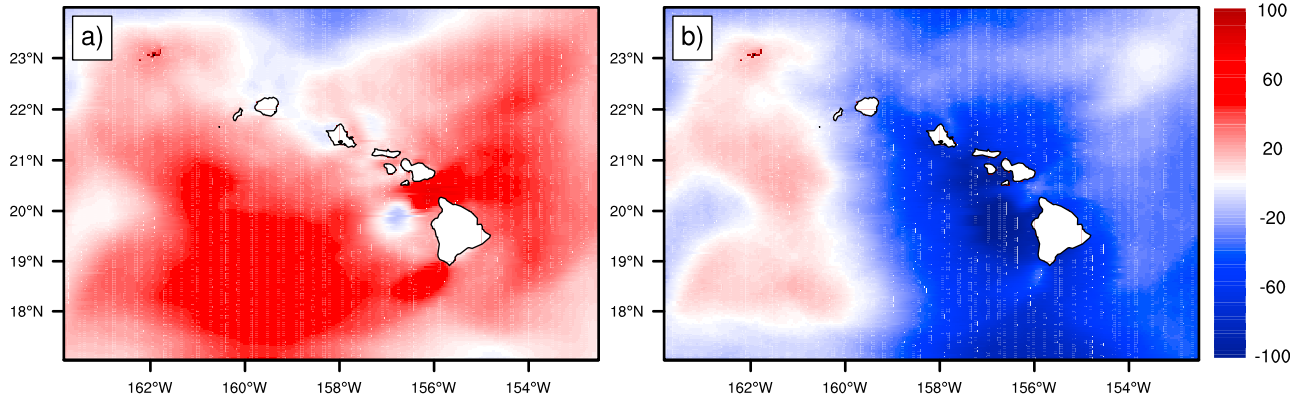


Figure 6. Time-averaged heat flux (W/m^2) adjustments made during the F09M and F09W experiments at (a) 14:00 and (b) 02:00 local time.

assumes that the errors are unbiased; however, comparison between the FWD case and observations show biased SST regions. The upper model layer used to represent SST is 4 m thick on average because our domain is deep (>5000 m) and ROMS uses a terrain following coordinate system. Satellite radiometers observe only the temperature of the skin layer of the ocean, rather than the bulk layer temperature that is representative of the upper few meters of the ocean. The thickness of the skin layer is less than a millimeter [Grassl, 1976] and contains a sharp temperature gradient when wind speeds are less than 10 m/s [Clauss *et al.*, 1970], above which wind induced waves destroy the skin layer. Differences between the skin and bulk temperatures (ΔT) measured more than a meter below the surface differ as much as 1 K [Robinson *et al.*, 1984] and can vary as much in a single diurnal cycle [Schluessel *et al.*, 1990]. Following Liu and Businger [1975], we estimate

$$\Delta T \approx Q_N \left(\frac{t_*}{\rho_w c_p \kappa} \right)^{\frac{1}{2}}, \quad (5)$$

where Q_N is the net surface heat flux, t_* is the surface renewal time scale, ρ_w is the density of seawater, c_p is the specific heat of the ocean at constant pressure and salinity, and κ is the molecular thermal conductivity. We calculated the bulk-skin temperature difference for data near 02:00 and 14:00 local time (the nominal time of MODIS passes) using the surface heat flux and wind stress from FWD. The temperature gradient between the bulk and skin layer is negligible except in the immediate lee of the islands where winds are reduced. The average daytime skin temperature is more than 0.2 K warmer than the bulk temperature in lee of the islands of Maui and Hawai'i, while at night, the skin is 0.1 K cooler than the bulk temperature.

[31] The bulk-skin temperature differences and 4 m representation of SST in the model lead to a bias between the observations and FWD. On average the FWD model is 0.3 K warmer than coincident SST observations, with large SST biases found in lee of the islands. The largest bias is found in the lee of the island of Hawai'i where it is on average 0.7 K (warmer than observations). In numerical experiments with model forcing from WRF, the incoming solar shortwave radiation flux is larger than that from MM5/NCEP forced

models, showing an average increase of 200 W/m^2 in peak daytime hours. The greater daytime heat flux increases the SST bias in FWD case to 1 K for several hundred kilometers leeward of the island of Hawai'i and in the Alenuihaha Channel.

[32] The assimilation effectively removes the SST biases in both the NF08, F09M, and F09W experiments to 0.03, 0.09, and 0.08 K, respectively, using different physical mechanisms. The NF08 experiment only adjusts initial conditions and has no other way to account for diurnal SST variability. Even so, the average SST bias from NF08 is smaller than that from F09M and F09W; however, this is due to the inducing of a cold bias in the NF08 system during peak daytime hours. Analysis of temperature observation-model RMSE from subsurface in situ data gives further insight into how SST observations are affecting the NF08 experiment. In the regions below 200 m, the reduction in RMSE and bias are similar between NF08 and F09M, with RMSE below 0.7 K and a cold bias less than 0.1 K. However, above 200 m depth both RMSE and bias from NF08 are higher than values from coincident cycles of FWD. The largest increase is over 1 K at 50 m depth in both RMSE and bias. The bias is unaffected in the F09M case and RMSE is below 0.7 K. Without surface forcing, the NF08 experiment generates upwelling in order to bring colder waters to the surface to compensate for the diurnal fluctuation of SST, leading to unrealistic and significantly colder temperatures in the upper 200 m layer.

[33] On the other hand, by adjusting the surface heat flux the F09M and F09W experiments have a time-dependent mechanism to account for some of the diurnal SST bias found between the model and observations. Here the cold, daytime bias is removed, as is the nighttime warm bias in the majority of the domain (except in the island channels and in lee of the island of Hawai'i where a warm bias of 0.2 K persists). Figure 6 shows time-averaged maps of the adjustments made to the heat flux at 14:00 and 02:00 local time. The daytime heat flux is increased over the majority of the domain by 25 W/m^2 , while at night the heat flux is reduced at some places by more than 100 W/m^2 , primarily in lee and south of the island of Hawai'i. The widespread distribution of the nighttime bias is likely due to the average 4 m thick layer used to represent SST diurnal variability in the model.

[34] In future assimilation experiments the model surface layer will ideally be significantly shallower. Also, models of upper ocean diurnal warming, such as the profiles of upper ocean heating (POSH) model developed by *Gentemann et al.* [2009], could be used to correct radiometric SST data for bulk-skin temperature differences prior to assimilation.

3.4. Salt Flux and Wind Stress Adjustments

[35] During both the F09M and F09W experiments salt flux and wind stress are also adjusted during the minimization procedure. When using WRF forcing, the FWD model evaporates 60% less as compared to when using MM5/NCEP. However, while the surface salt flux is adjusted only 3% in the F09M experiment (with larger reductions of 10%–15%) in the lee of Hawai'i), during F09W the salt flux is reduced by 30% over the entire domain. This result is counterintuitive and is likely a response to the increased heat flux from WRF.

[36] Time-averaged mean wind stress computed from MM5/NCEP and WRF models have similar values in both direction and magnitude, though the variability is higher in WRF case. Surface wind stress is relatively unchanged during the assimilation in both experiments. In F09M, westward zonal wind stress due to the trade winds is unaffected over a majority of the domain and reduced by only 2%–3% in the Alenuihaha Channel and south of Hawai'i. Meridional wind stress is increased north of the island chain by 5%–10% and relatively unaffected elsewhere. Similar changes are found in the F09W experiment; however, without the northward increase in wind stress.

3.5. Comparing Coincident Assimilations With and Without Forcing Adjustment

[37] In the results presented in section 3.3, we show that without surface forcing adjustment, the assimilation degrades the temperature structure at depth. Because there is no temporal overlap between the NF08 and F09M/F09W experiments, we performed an additional experiment to compare both assimilation configurations over the same time period. We assimilated only satellite data and withhold the in situ observations as an independent validation over 6 assimilation cycles from 17 July 2009 to 6 August 2009. During this time a relatively large SST RMSE between the model and observations exists, which should maximize the subsurface effects when not allowing adjustments to the surface forcing. Also during this time both atmospheric products were available, so the initial 3 cycles used MM5/NCEP forcing and the final 3 use WRF. In this section we refer to these two experiments as, EXNF, which refers to the assimilation analyses with only initial condition correction, and EXF, which refers to analyses with both initial condition and surface forcing correction.

[38] The reduction in SST RMSE in the EXNF and EXF experiments is nearly identical for each of the MM5/NCEP and WRF periods. However, the mean bias between SST observations and the forecast circulations is increased by 0.2 K because of the increased heat flux from the WRF model during those cycles.

[39] We compare against observations from a Seaglider mission north of O'ahu to examine the subsurface temperature fields from the EXNF and EXF experiments. In the initial cycle, the mean temperature profile from the

observations matches the mean profile from both EXNF and EXF; however, after each subsequent cycle, EXNF is increasingly colder than the observations. This is most apparent in depths from 140 m to 220 m, where a cool 1.5 K bias first develops, then increases to more than 3 K from 40 m to 200 m in the final cycle of the experiment. This is accompanied with an increase in RMSE above 200 m depth in the EXNF experiment that is not found in EXF. In the EXF experiment, a minor increase is found in RMSE of less than 0.5 K in the 4th and 6th cycle, but no change above 200 m exists. This is a similar pattern to that found in the NF08 experiment, with an increase in temperature bias and RMSE at the 40–160 m layer.

3.6. Impact of Assimilation on Mixed Layer Depths

[40] We have shown that the assimilation of SST observations without surface forcing adjustment affects the subsurface structure of temperature in the model; however, the largest effects have been limited to depths below 40 m. We explore the effects of the assimilation on the mixed layer depth (MLD) in this section. A cold bias exists in the NF08 experiment at depths between 40 m and 200 m that suggest colder waters are shoaled. F09M/W should have less impact upon the MLD as the atmospheric forcing adjustment provides the means to match the SST. We calculate the MLD using the finite difference criteria method from a near-surface reference depth of 10 m. We use a 0.2°C temperature difference as the criterion to define the MLD, as suggested by *de Boyer Montégut et al.* [2004]. This method and temperature criterion are also used to generate MLD climatologies from the Asia-Pacific Data-Research Center (APDRC) that are compared with the results from FWD, NF08, F09M, and F09W. The MLD climatology is made a regular 2° by 2° grid for every month and was generated from over 60 years of high vertical resolution profiling data.

[41] The MLD climatology shows a seasonal variation that ranges from less than 40 m in April to more than 75 m in November. The seasonal signal is suppressed near the island and the MLD is shoaled as compared to abyssal waters. Figure 7a shows the spatially and temporally averaged MLD values per cycle for abyssal waters from the climatology and experiments, while Figure 7b shows the spatially averaged values for near island waters. The experiments capture the seasonal signal in both abyssal waters and coastal-leeward waters, though is deeper in the winter and shallower in summer. The largest reductions in MLD are in the NEC, where the F09M and F09W MLD is more than 30 m shallower than those from the FWD experiment. Spatially averaged MLDs from F09 cases shown in Figures 7a and 7b demonstrate a similar seasonal pattern to that found in climatology and the FWD experiment. Overall, the MLD from the assimilation experiments better matches the climatological MLD with the FWD MLD extending too deep during the winter months.

3.7. Impact of Assimilation on Tidal Energy

[42] It is not possible for a model to perfectly reproduce the tidal dynamics of the observations in regions where barotropic tides interact strongly with the topography and generate baroclinic tides. This is because of the differing bathymetric representation of a model, as well as the pseudorandom phase shifts in the baroclinic tides due to density

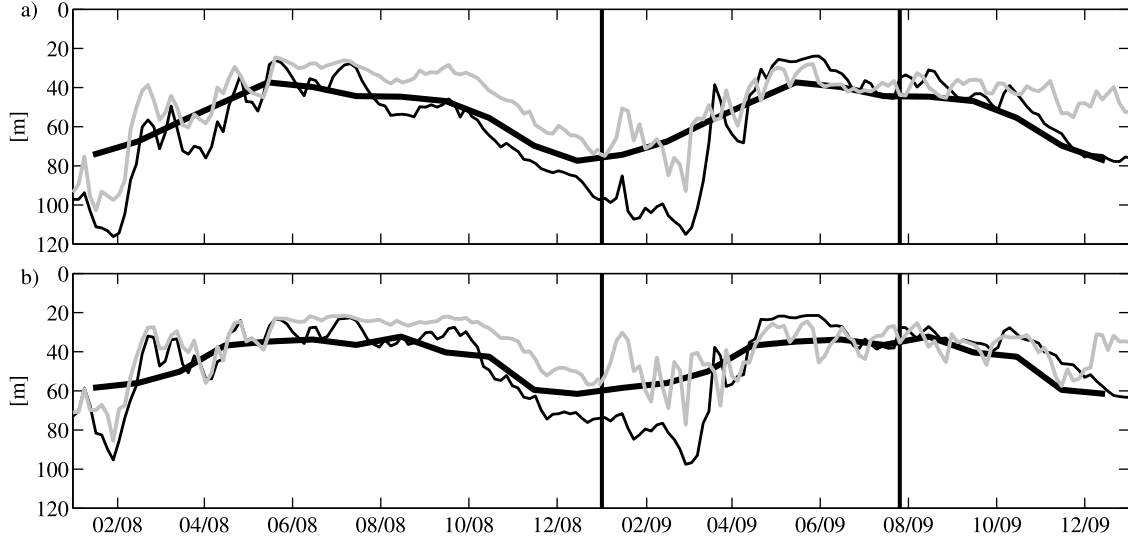


Figure 7. Mixed layer depths from (a) abyssal waters and (b) leeward-coastal waters from climatology (thick black line), the FWD experiment (thin black line), and the NF08/F09M/F09W experiments (thin grey line). Vertical lines are as in Figure 2.

variations. To assimilate SSH observations one must remove their tidal signal, then add back tidal information from the model. We explore the effects of the assimilation adjustments to both the barotropic and baroclinic tidal dynamics in this section. The assimilation system was not configured to

improve the tidal flow directly; however, relatively small changes should be seen if the system is working correctly.

[43] To examine possible effects of the assimilation on the spatial structure of the surface expression of the tides we focus on the dominant semidiurnal (M_2) tide, calculating the

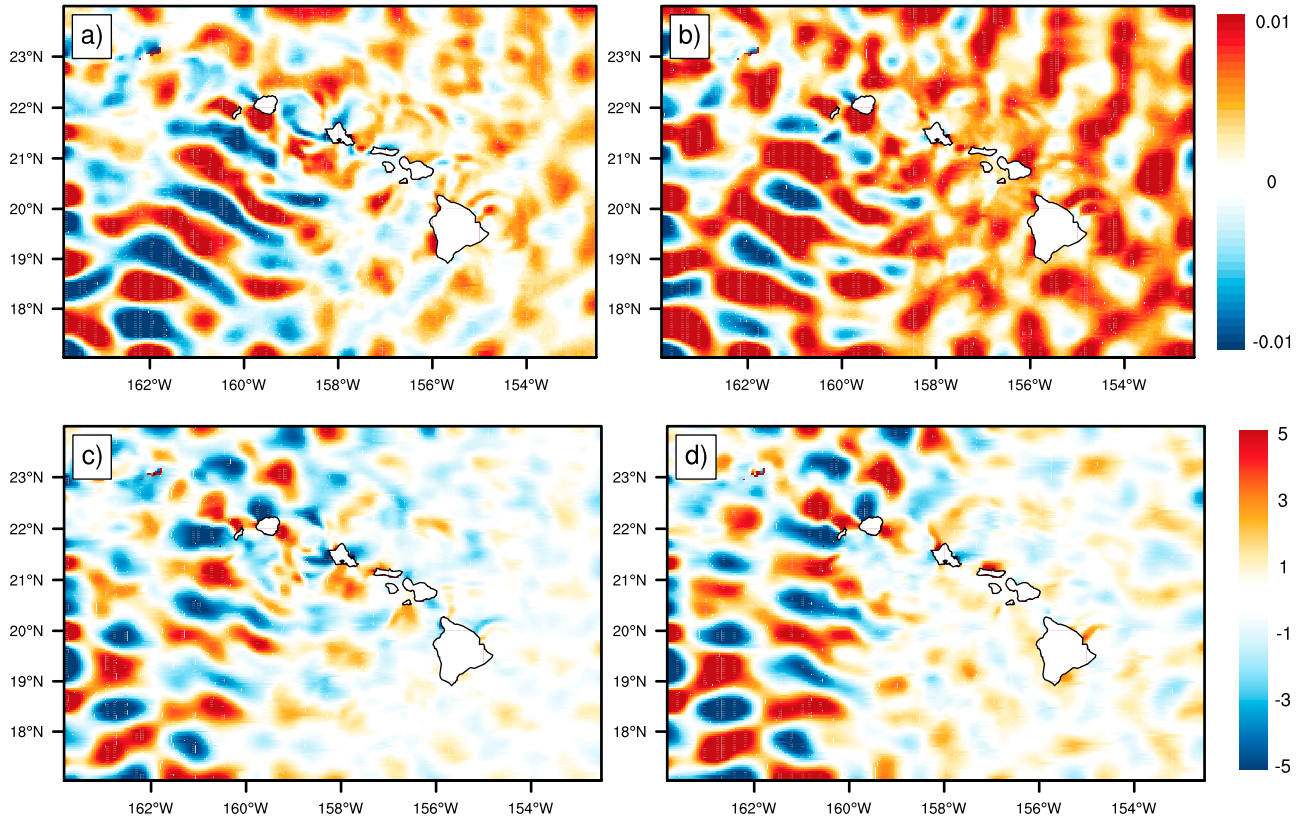


Figure 8. Time-averaged M_2 tidal amplitude (m) and phase (degrees) differences between assimilation experiments and the FWD case: (a) amplitude difference (NF08–FWD), (b) phase difference (NF08–FWD), (c) amplitude difference (F09M/F09W–FWD), and (d) phase difference (F09M/F09W–FWD).

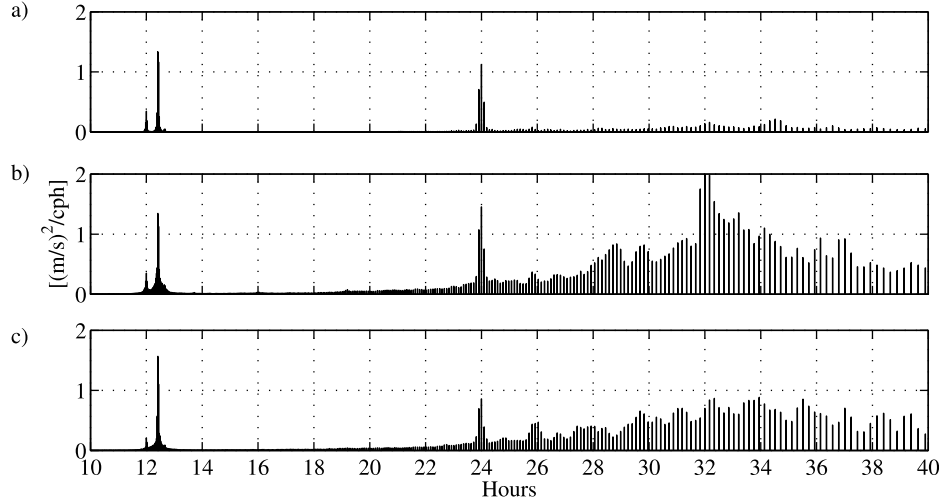


Figure 9. Spatially averaged power spectral density for time series of surface baroclinic zonal velocities in the (a) FWD, (b) NF08, and (c) F09M/F09W experiments.

phases and amplitudes from the four experiments. The internal tides reflect off of the surface; hence, the free surface does not provide a purely barotropic tidal signal. Figures 8a and 8b show the changes in amplitude and phase made during the NF08 and F09M assimilation experiments. The changes in phase due to the assimilation are negligible in the eastern half of the domain. This is to be expected, as the baroclinic energy flux emanates south-southwest from Kaena Ridge and south from French Frigate Shoals [Rainville et al., 2010]. In these directions, extending from the islands of O'ahu and Kaua'i, the baroclinic tides are shifted in phase during the assimilation by as much as 5° (over 10 min) and in amplitude by 1 cm (10%–20% of the M_2 amplitude) because of variations in the vertical density structure and mesoscale currents in the analysis.

[44] We generate time series of surface baroclinic zonal velocities by subtracting the depth-averaged velocity from the surface current and, in the case of the assimilation experiments, omit the initial increments to analyze the baroclinic spectrum for each experiment. Space averaged power spectral density (PSD) from the time series generated from FWD, NF08 and FA9(M/W) experiments all contain narrow-band peaks in energy at the S_2/M_2 , N_2 , S_1 , K_1 , and O_1 frequencies (Figure 9); however, with slightly different energy levels. The PSDs show a transfer of energy from the tidal frequencies to the surrounding harmonics due to changes in the stratification made during the assimilation that are not present in the FWD experiment. Varying stratification associated with mesoscale currents impacts the propagation of internal tides [Park and Watts, 2006] and the resulting phase and amplitude modulation smears the energy out of phase-locked signals [Chavanne et al., 2010]. This transfer of energy is highest in the NF08 run where, as previously discussed, greater increments are made to the density field.

3.8. Impact of Assimilation on Inertial Energy

[45] Figure 9 reveals significant increases in energy levels in assimilation experiments from 20 to 48 h that peak in the inertial period range for the domain (29–41 h for the region). The amplitudes of these oscillations are an order of

magnitude larger in assimilation experiments, when compared to FWD, and vary in period latitudinally consistent with inertial motions. PSDs of the free surface and depth averaged velocities from assimilation experiments show no increase in energy in this period range, when compared to FWD, suggesting the oscillations are purely baroclinic. Such spurious inertial oscillations have been reported in both meteorological [Polavarapu et al., 2000] and oceanic [Lea et al., 2006] variational data assimilation studies and are associated with ageostrophic imbalances in the initial conditions from the IS4D-Var increment.

[46] The PSDs shown in Figure 9 clearly demonstrate that there are strong oscillations in inertial periods in the assimilation experiments, however, they provide little insight into the behavior or generation mechanisms. We must use non-Fourier-based analysis to estimate the localized phase and amplitude of the oscillations because of the discrete signal change after each assimilation cycle. The continuous wavelet transform (CWT) has been shown to be useful in capturing nonstationary high-frequency signals in the ocean [Flinchem and Jay, 2000], giving the evolution of signal characteristics through the data set. Figure 10a shows a representative time series of surface zonal velocities from a single point in the center of the domain from both the FWD and NF08 experiments. We ensure that any increase in inertial oscillations are not generated by adjustments to wind stress possible in the FA09M/W experiments by using a time series from the NF08 experiment. Figures 10b and 10c show wavelet scalograms from tenth-order Gaussian CWT of the FWD and NF08 surface zonal velocity time series. The Gaussian wavelet is chosen because of its flexibility in time and frequency resolution. In the FWD wavelet scalogram there is a continuity of energy at 12 and 24 h from the semi and diurnal tidal constituents, along with intermittent increases in wave amplitudes around inertial periods having maximum values of 35 cm/s. Similar energy at the diurnal and semidiurnal tidal periods is present in the scalogram from the NF08 time series, however, at inertial periods in the NF08 scalogram wave amplitudes close to 75 cm/s are common. The variability in the NF08 time series is much

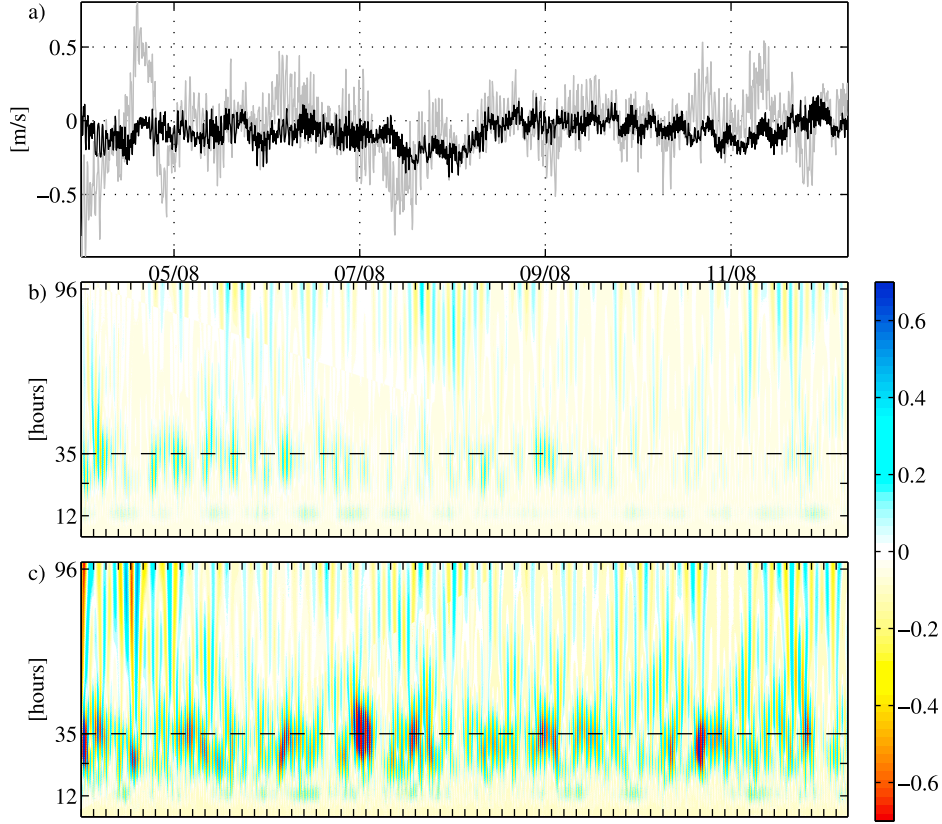


Figure 10. (a) Example time series of the surface zonal velocity from FWD (black) and NF08 (grey) experiments at 158.96°W, 19.69°N. (b) Amplitude scalogram (m/s) for the surface zonal velocity time series from FWD using a tenth-order Gaussian wavelet. Ticks along the x axis indicate the beginning of each assimilation cycle. The inertial frequency for the latitude (35 h) is marked by the dashed line. (c) Same as Figure 10b but from the NF08 time series.

larger than FWD, with a standard deviation of over 23 cm/s, compared to 14 cm/s in the FWD case, and the scalograms suggest that the increased variability is focused in the inertial spectral band.

[47] Comparing CWT scalograms generated from surface velocity time series from other parts of the domain in the NF08, F09M, and F09W experiments suggests that spurious inertial oscillations are commonly generated during the assimilation using both configurations. However, the spurious inertial oscillations are significantly damped in shallow waters near the island chain. The timing and locations of the increases in inertial wave amplitudes suggests that the spurious oscillations are associated with large increments applied at the surface in response to assimilating either SSH or SST observations. To verify this we conducted an additional experiment that assimilated only SSH or SST data, and found spurious inertial oscillations in both cases. Also, in this short test, from assimilating SST only the oscillations were more pronounced than when compared to assimilating SSH only.

[48] In future assimilation experiments, the balanced initialization feature within ROMS could be used to limit the generation of spurious inertial oscillations in the assimilation experiments. The balance operator algorithm follows the methodology of *Weaver and Courtier* [2001] to constrain the error covariance by establishing linear, geostrophically balanced relationships between state variables. However, it

utilizes an elliptical solver that may limit its effectiveness in an island domain. Also, because any discrete change to a continuous system will radiate energy, to fully dampen the spurious inertial oscillations requires a digital filter as has been shown in numerical weather prediction, such as that described by *Polavarapu et al.* [2000].

3.9. Impact of Assimilation on Low-Frequency Dynamics

[49] We examine the impact of high-frequency variability added to the assimilation experiments via inertial oscillations on the low-frequency eddy kinetic energy (EKE) in the NF08, F09M, and F09W experiments in this section. EKEs are calculated from the average surface velocity fields of each 4 day experiment cycle to filter out tides, inertial oscillations, and other high-frequency signals. We then compare our results with EKE estimates from the AVISO weekly mapped absolute geostrophic current (AGC) product. The AGC fields are generated by optimally interpolating along-track altimetry data and represent only geostrophic velocity, hence, the EKE from AGC should underestimate the true variability in the ocean. Figure 11a shows the spatially averaged EKE per experiment cycle from FWD and assimilation cases along with the average EKE from AGC over the entire domain. EKE values from AGC show no trend, maintaining a constant value of 100 (cm/s)². FWD

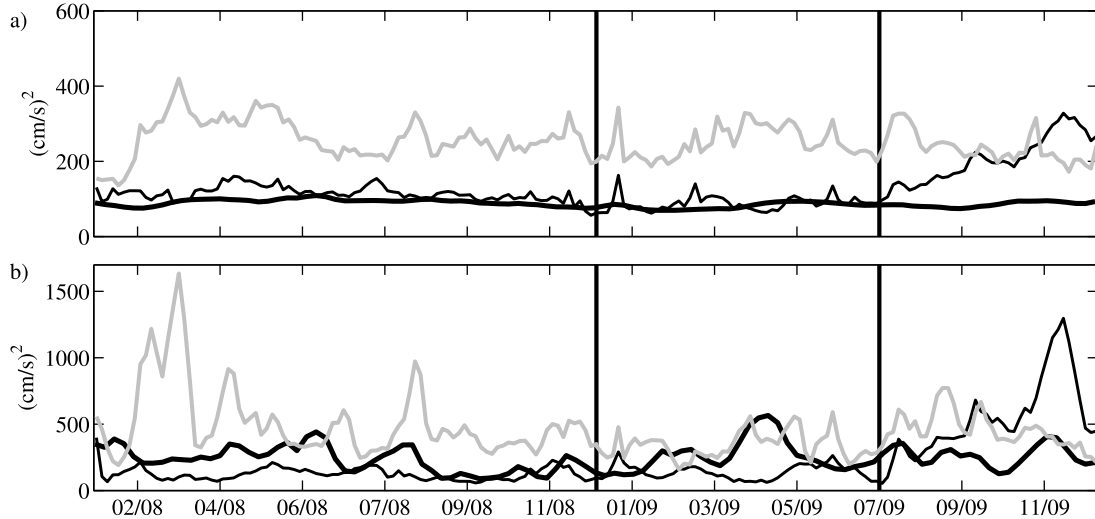


Figure 11. Spatially averaged eddy kinetic energy (EKE; $(\text{cm/s})^2$) per experiment cycle from the FWD (thin black line) and NF08/F09M/F09W experiments (thin grey line) and the Archiving Validation and Interpretation of Satellite Oceanographic data (AVISO) absolute geostrophic currents product (thick black line). (a) Spatially averaged EKE over the entire domain and (b) only the region in lee of the island of Hawaii (19°N – 21°N and 156°W – 158.5°W).

EKE agrees in magnitude with that from AGC until the change to WRF forcing in late July 2009. Eddies formed in lee of the Hawaii dramatically increase EKE, because of this, we also show mean EKE from in lee of Hawaii to 158.5°W (Figure 11b). EKE values from AGC in lee of Hawaii vary in time, ranging from 100–600 $(\text{cm/s})^2$. FWD case EKE values, in the leeward region, when using MM5/NCEP forcing are less than those from AGC. This suggests that the nonlinear model is underestimating the EKE when forced by MM5/NCEP fields. Average EKE values from the entire domain increases gradually to more than double those from AGC after the change to WRF forcing, and in lee to more than 6 times those from AGC.

[50] After the first few cycles, average EKE values for the entire domain in assimilation experiments range between 200 $(\text{cm/s})^2$ and 400 $(\text{cm/s})^2$, 2–4 times more than EKE values from AGC. In assimilation experiments the increase in leeward EKE, relative to the domain average, compares well with the leeward increase from AGC. EKE values over the entire domain from the NF08 experiment are slightly larger than those from F09M/F09W. Leeward EKE values in the NF08 experiment spike to over 900 $(\text{cm/s})^2$. These increases are not present in the F09M and F09W experiments and are likely due to increased variability generated in the model via the increment in the NF08 experiment. Also, the large increase in EKE in the FWD experiment, after the change to WRF forcing, is not seen in assimilation experiments, as EKE values maintain a range of 200–300 $(\text{cm/s})^2$ over the domain and 400–700 $(\text{cm/s})^2$ in lee during this time period. The EKE levels from assimilation experiments agree well with estimates from eddy-resolving ocean general circulation models [Noh *et al.*, 2007].

4. Conclusions

[51] We have explored the behavior of a four-dimensional variational data assimilation system applied to the Hawaiian

Island region by using two assimilation configurations, with and without surface forcing adjustment, and two atmospheric forcing products, a combination of NCEP/MM5 and WRF. All available observations were assimilated including satellite altimetry and radiometry, and in situ temperature and salinity profiles collected from autonomous Seagliders, Argo floats, and shipboard CTD. We found significant reductions in misfit RMSE are made between the model and SST (23%–51%) and salinity (29%–47%) observations, when compared against a control run without data assimilation, from both assimilation configurations, using either atmospheric forcing product. The RMSE between all assimilation experiments and SST observations approached the average observational error of 0.31 K, except in lee of Hawai'i, where reduced horizontal decorrelation length scales, as well as increased variability limited the reduction of RMSE to 0.6 K. Improvements in RMSE with regard to the high-resolution, along-track SSH observations were limited to 13%–14% because of underestimated SSH observational error and the inclusion of tidal signals when calculating the prior background covariance. The use of low-resolution, real-time, along-track data further limited the reductions of SSH RMSE within the assimilation to less than 4%.

[52] The configuration of the assimilation system had a large effect on the subsurface temperature structure. Reductions of RMSE, compared against the control run, between the model and in situ temperature observations were limited to 6% when adjusting only initial conditions. These reductions in RMSE improved to 28% if atmospheric forcing was also adjusted during assimilation. This was due to the inability of the assimilation system to respond to diurnal biases between the modeled and observed SST without atmospheric adjustments in time. The assimilation system degrades the temperature structure in the interior of the ocean by unrealistically cooling waters below the mixed layer (from 40 m to 200 m) if only initial conditions were

adjusted. The depth of the mixed layer was slightly shoaled during the assimilation using both configurations, however, showed better agreement with climatology in the region, compared to the control run without data assimilation. When atmospheric forcing was also adjusted during the assimilation procedure there was no evidence of incorrect subsurface cooling, as the adjustment of heat flux in time was able to account for diurnal SST biases. Along with heat flux, there were salt flux and wind stress adjustments during the assimilation; however, only relatively small changes were made.

[53] Baroclinic tides in the analysis were modified during assimilation by 10%–20% in amplitude and over 10 min in phase in regions where internal tide generation occurs. The modifications were due to changes in the density structure that affected the surface expression of the baroclinic tides. The overall energies of surface baroclinic tides were minimally affected during the assimilation, however, some small transfer of energy from tidal frequencies to surrounding harmonics were found at semi and diurnal bands.

[54] Significant spurious inertial oscillations were found in assimilation dynamics because of imbalances in initial conditions from the IS4D-Var increment. These oscillations were associated with the assimilation of both, or either, SSH and SST observations. However, these oscillations found in assimilation fields showed little effect on the low-frequency variability. The overall flow of the region was maintained and an improvement to the EKE in the immediate lee of the island of Hawai'i was achieved. This increase in EKE better reflected the generation of eddies that shed in the lee of the island; however, the assimilation increased the EKE over the entire domain to more than is observed.

[55] We have shown that over 4 day period, IS4D-Var is effective at submesoscale resolution in the presence of strong barotropic flow with significant energy conversion into the baroclinic tides. The assimilation was able to balance a majority of SST observations with a limited set of in situ observations that captured these baroclinic tides. Amidst these processes, the results show that over a wide variety of dynamical length and time scales, the 4D-Var solution is consistent with the observations.

[56] **Acknowledgments.** We wish to thank the editor and two anonymous reviewers for improving this paper. D. Matthews was supported by NOAA grant NA07NOS4730207, B. S. Powell was supported by the Office of Naval Research grant N00014-09-10939, and I. Janečković was supported by NOAA grant NA10NOS4730016. The authors would also like to thank Glenn Cater for providing Seaglider observational data and Roger Lukas for providing Hawai'i Ocean Time-series observations, which are supported by the U.S. National Science Foundation under grant OCE-0327513. This is SOEST publication 8529. The authors would like to thank Y.-L. Chen of the Department of Meteorology for the MM5 and WRF atmospheric model data.

References

- Akima, H. (1984), On estimating partial derivatives for bivariate interpolation of scattered data, *Rocky Mt. J. Math.*, 14(1), 41–52.
- Barron, C. N., C. A. Kara, P. J. Martin, R. C. Rhodes, and L. F. Smedstad (2006), Formulation, implementation and examination of vertical coordinate choices in the Global Navy Coastal Ocean Model (NCOM), *Ocean Modell.*, 11, 347–375.
- Broquet, G., C. A. Edwards, A. Moore, B. S. Powell, M. Veneziani, and J. D. Doyle (2009), Application of 4D-varational data assimilation to the California Current System, *Dyn. Atmos. Oceans*, 48, 69–92.
- Broquet, G., A. M. Moore, H. G. Arango, and C. A. Edwards (2011), Corrections to ocean surface forcing in the California Current System using 4D variational data assimilation, *Ocean Modell.*, 36, 116–132.
- Calil, P. H., K. J. Richards, Y. Jia, and R. R. Bidigare (2008), Eddy activity in the lee of the Hawaiian Islands, *Deep Sea Res., Part II*, 55, 1179–1194.
- Carter, G. S., M. A. Merrifield, J. M. Becker, K. Katsumata, M. C. Gregg, D. S. Luther, M. D. Levine, T. J. Boyd, and Y. L. Firing (2008), Energetics of M_2 barotropic-to-baroclinic tidal conversion at the Hawaiian Islands, *J. Phys. Oceanogr.*, 38, 2205–2223.
- Chapman, D. C. (1985), Numerical treatment of cross-shelf open boundaries in a barotropic coastal ocean model, *J. Phys. Oceanogr.*, 15, 1060–1075.
- Chavanne, C., P. Flament, G. Carter, M. A. Merrifield, and S. D. Luther (2010), The surface expression of semidiurnal internal tides near a strong source at Hawaii. Part I: Observations and numerical predictions, *J. Phys. Oceanogr.*, 40, 1155–1179.
- Chen, S., and B. Qiu (2010), Mesoscale eddies northeast of the Hawaiian archipelago from satellite altimeter observations, *J. Geophys. Res.*, 115, C03016, doi:10.1029/2009JC005698.
- Chiswell, S. M. (1994), Vertical structure of the baroclinic tides in the central north Pacific subtropical gyre, *J. Phys. Oceanogr.*, 24, 2032–2039.
- Clauss, E., H. Hinzpeter, and J. Muller-Glewe (1970), Measurements of the temperature structure in the water at the interface between the ocean-atmosphere, *Meteor Forschungsber. Reihe B*, 5, 90–94.
- Courtier, P., J. N. Thépaut, and A. Hollingsworth (1994), A strategy for operational implementation of 4D-Var, using an incremental approach, *Q. J. R. Meteorol. Soc.*, 120, 1367–1387.
- de Boyer Montégut, C., G. Madec, A. S. Fischer, A. Lazar, and D. Iudicone (2004), Mixed layer depth over the global ocean: An examination of profile data and a profile-based climatology, *J. Geophys. Res.*, 109, C12003, doi:10.1029/2004JC002378.
- Desroziers, G., L. Berre, V. Chabot, and B. Chapnik (2009), A posteriori diagnostics in an ensemble of perturbed analyses, *Mon. Weather Rev.*, 137, 3420–3436.
- Egbert, G. D., A. F. Bennett, and M. G. G. Foreman (1994), TOPEX/POSEIDON tides estimated using a global inverse model, *J. Geophys. Res.*, 99, 24,821–24,852.
- Fairall, C. W., E. F. Bradley, D. P. Rogers, J. B. Edson, and G. S. Young (1996), Bulk parameterization of air-sea fluxes for tropical ocean-global atmosphere Coupled-Ocean Atmosphere Response Experiment, *J. Geophys. Res.*, 101, 3747–3764.
- Fisher, M. (1998), Minimization algorithms for variational data assimilation, paper presented at Seminar on Recent Developments in Numerical Methods for Atmospheric Modelling, Eur. Cent. for Medium-Range Weather Forecasts, Reading, U. K.
- Flament, P., S. Kennan, R. Lumpkin, M. Sawyer, and E. Stroup (1998), *The Ocean Atlas of Hawaii*, Univ. of Hawaii Press, Honolulu.
- Flinchem, E. P., and D. A. Jay (2000), An introduction to wavelet transform tidal analysis methods, *Estuarine Coastal Shelf Sci.*, 51(2), 177–200.
- Gentemann, C. L., P. J. Minnett, and B. Ward (2009), Profiles of ocean surface heating (POSH): A new model of upper ocean diurnal warming, *J. Geophys. Res.*, 114, C07017, doi:10.1029/2008JC004825.
- Grassl, H. (1976), A new type of absorption in the atmospheric infrared window due to water vapor polymers, *Beitr. Phys. Atmos.*, 49(4), 225–236.
- Karl, D. M., and R. Lukas (1996), The Hawaii Ocean Time-Series (HOT) program: Background, rationale and field implementation, *Deep Sea Res., Part II*, 43, 129–156.
- Large, W. G., J. C. McWilliams, and S. C. Doney (1994), Oceanic vertical mixing: A review and a model with a nonlocal boundary layer parameterization, *Rev. Geophys.*, 32, 363–404.
- Lea, D. J., T. W. N. Haine, and R. F. Gasparovic (2006), Observability of the Irminger Sea circulation using variational data assimilation, *Q. J. R. Meteorol. Soc.*, 132(618), 1545–1576.
- Liu, W. T., and J. A. Businger (1975), Temperature profile in the molecular sublayer near the interface of a fluid in turbulent motion, *Geophys. Res. Lett.*, 2, 403–404.
- Lorenc, A. (2006), Why does 4D-Var beat 3D-Var?, *Q. J. R. Meteorol. Soc.*, 131, 3247–3257.
- Lumpkin, C. (1998), Eddies and currents of the Hawaiian islands, PhD dissertation, Sch. of Ocean and Earth Sci., Univ. of Hawai'i at Mānoa, Honolulu.
- Marchesiello, P. (2001), Open boundary conditions for long-term integration of regional oceanic models, *Ocean Modell.*, 3, 1–20.
- Matthews, D., B. Powell, and R. Milliff (2011), Dominant spatial variability scales from observations around the Hawaiian islands, *Deep Sea Res., Part I*, 58(10), 979–987.
- McClain, E. P., W. G. Pichel, and C. C. Walton (1985), Comparative performance of AVHRR-based multichannel sea surface temperatures, *J. Geophys. Res.*, 90, 11,587–11,601.
- Merrifield, M. A., P. E. Holloway, and T. M. S. Johnston (2001), The generation of internal tides at the Hawaiian Ridge, *Geophys. Res. Lett.*, 28, 559–562.

- Milliff, R. F., J. Morzel, D. B. Chelton, and M. H. Freilich (2004), Wind stress curl and wind stress divergence biases from rain effects on QSCAT surface wind retrievals, *J. Atmos. Oceanic Technol.*, 21, 1216–1231.
- Moore, A. M., H. G. Arango, E. D. Lorenzo, B. D. Cornuelle, A. J. Miller, and D. J. Neilson (2004), A comprehensive ocean prediction and analysis system based on the tangent linear and adjoint of a regional ocean model, *Ocean Modell.*, 7, 227–258.
- Moore, A. M., H. G. Arango, G. Broquet, C. Edwards, M. Veneziani, B. S. Powell, D. Foley, J. Doyle, D. Costa, and P. Robinson (2011a), The Regional Ocean Modeling System (ROMS) 4-dimensional variational data assimilation systems: Part II—Performance and application to the California Current System, *Prog. Oceanogr.*, 91, 50–73.
- Moore, A. M., H. G. Arango, G. Broquet, C. Edwards, M. Veneziani, B. S. Powell, D. Foley, J. Doyle, D. Costa, and P. Robinson (2011b), The Regional Ocean Modeling System (ROMS) 4-dimensional variational data assimilation systems: Part III—Observation impact and observation sensitivity in the California Current System, *Prog. Oceanogr.*, 91, 74–94.
- Moore, A. M., H. G. Arango, G. Broquet, B. S. Powell, J. Zavala-Garay, and A. T. Weaver (2011c), The Regional Ocean Modeling System (ROMS) 4-dimensional variational data assimilation systems: Part I—System overview and formulation, *Prog. Oceanogr.*, 91, 34–49.
- Noh, Y., B. Y. Yim, S. H. You, J. H. Yoon, and B. Qiu (2007), Seasonal variation of eddy kinetic energy of the North Pacific Subtropical Counter-current simulated by an eddy-resolving OGCM, *Geophys. Res. Lett.*, 34, L07601, doi:10.1029/2006GL029130.
- Oka, E., and K. Ando (2004), Stability of temperature and conductivity sensors of Argo profiling floats, *J. Oceanogr.*, 60(2), 253–258.
- Park, J.-H., and D. R. Watts (2006), Internal tides in the southwestern Japan/East Sea, *J. Phys. Oceanogr.*, 36, 22–34.
- Polavarapu, S., M. Tanguay, and L. Fillion (2000), Four-dimensional variational data assimilation with digital filter initialization, *Mon. Weather Rev.*, 128, 2491–2510.
- Powell, B. S., H. G. Arango, A. M. Moore, E. Di Lorenzo, R. F. Milliff, and D. Foley (2008), 4DVAR data assimilation in the Intra-Americas Sea with the Regional Ocean Modeling System (ROMS), *Ocean Modell.*, 25, 173–188.
- Powell, B. S., A. M. Moore, H. G. Arango, R. F. Milliff, and R. R. Leben (2009), Real-time assimilation and prediction in the Intra-Americas Sea with the Regional Ocean Modeling System (ROMS), *Dyn. Atmos. Oceans*, 48, 46–68.
- Rainville, L., T. M. S. Johnston, G. S. Carter, M. A. Merrifield, R. Pinkel, P. F. Worcester, and B. D. Dushaw (2010), Interference pattern and propagation of the M_2 internal tide south of the Hawaiian Ridge, *J. Phys. Oceanogr.*, 40, 311–325.
- Ray, R. D., and G. T. Mitchum (1996), Surface manifestation of internal tides generated near Hawaii, *Geophys. Res. Lett.*, 23, 2101–2104.
- Robinson, I. S., N. C. Wells, and H. Charnock (1984), The sea surface thermal boundary layer and its relevance to the measurement of sea surface temperature by airborne and spaceborne radiometers, *Int. J. Remote Sens.*, 5(1), 19–45.
- Schlüssel, P., W. J. Emery, H. Grassl, and T. Mammen (1990), On the bulk-skin temperature difference and its impact on satellite remote sensing of sea surface temperature, *J. Geophys. Res.*, 95, 13,341–13,356.
- Shchepetkin, A. F., and J. C. McWilliams (2005), The Regional Oceanic Modeling System: A split-explicit, free-surface, topography-following-coordinate ocean model, *Ocean Modell.*, 9, 347–404.
- Smith, R. B., and V. Grubii (1993), Aerial observations of Hawaii's wake, *J. Atmos. Sci.*, 50, 3728–3750.
- Talagrand, O., and P. Courtier (1987), Variational assimilation of meteorological observations with the adjoint vorticity equation. I: Theory, *Q. J. R. Meteorol. Soc.*, 113, 1311–1328.
- Weaver, A., and P. Courtier (2001), Correlation modelling on the sphere using generalized diffusion equation, *Q. J. R. Meteorol. Soc.*, 127, 1815–1846.
- Xie, S.-P., W. Liu, Q. Liu, and M. Nonaka (2001), Far-reaching effects of the Hawaiian Islands on the Pacific ocean–atmosphere system, *Science*, 292(5524), 2057–2060.
- Yang, Y., Y.-L. Chen, and F. M. Fujioka (2008a), Effects of trade-wind strength and direction on the leeside circulations and rainfall of the island of Hawaii, *Mon. Weather Rev.*, 136, 4799–4818.
- Yang, Y., S.-P. Xie, and J. Hafner (2008b), Cloud patterns lee of Hawaii Island: A synthesis of satellite observations and numerical simulation, *J. Geophys. Res.*, 113, D15126, doi:10.1029/2008JD009889.
- Yoshida, S., B. Qiu, and P. Hacker (2010), Wind generated eddy characteristics in the lee of the island of Hawaii, *J. Geophys. Res.*, 115, C03019, doi:10.1029/2009JC005417.
- Zanifé, O. Z., P. Vincent, L. Amarouche, J. P. Dumont, P. Thibaut, and S. Labroue (2003), Comparison of the Ku-band range noise level and the relative sea-state bias of the Jason-1, TOPEX, and Poseidon-1 radar altimeters, *Mar. Geod.*, 26, 201–238.
- Zhang, W. G., J. L. Wilkin, and H. G. Arango (2010), Towards an integrated observation and modeling system in the New York Bight using variational methods. Part I: 4DVAR data assimilation, *Ocean Modell.*, 35, 119–133.

I. Janečković, D. Matthews, and B. S. Powell, Department of Oceanography, University of Hawai'i at Mānoa, Marine Sciences Building, 1000 Pope Rd., Honolulu, HI 96822, USA. (ivica@soest.hawaii.edu; matthews@hawaii.edu; powellb@hawaii.edu)